Accelerated discovery of CO_2 electrocatalysts using active machine learning

https://doi.org/10.1038/s41586-020-2242-8

Received: 14 April 2018

Accepted: 13 March 2020

Published online: 13 May 2020

Check for updates

Miao Zhong[1,2,9], Kevin Tran[3,9], Yimeng Min[1,9], Chuanhao Wang[1,9], Ziyun Wang[1], Cao-Thang Dinh[1], Phil De Luna[4,8], Zongqian Yu[3], Armin Sedighian Rasouli[1], Peter Brodersen[5], Song Sun[6], Oleksandr Voznyy[1], Chih-Shan Tan[1], Mikhail Askerka[1], Fanglin Che[1], Min Liu[1], Ali Seifitokaldani[1], Yuanjie Pang[1], Shen-Chuan Lo[7], Alexander Ip[1], Zachary Ulissi[3]✉ & Edward H. Sargent[1]✉

The rapid increase in global energy demand and the need to replace carbon dioxide (CO_2)-emitting fossil fuels with renewable sources have driven interest in chemical storage of intermittent solar and wind energy[1,2]. Particularly attractive is the electrochemical reduction of CO_2 to chemical feedstocks, which uses both CO_2 and renewable energy[3–8]. Copper has been the predominant electrocatalyst for this reaction when aiming for more valuable multi-carbon products[9–16], and process improvements have been particularly notable when targeting ethylene. However, the energy efficiency and productivity (current density) achieved so far still fall below the values required to produce ethylene at cost-competitive prices. Here we describe Cu-Al electrocatalysts, identified using density functional theory calculations in combination with active machine learning, that efficiently reduce CO_2 to ethylene with the highest Faradaic efficiency reported so far. This Faradaic efficiency of over 80 per cent (compared to about 66 per cent for pure Cu) is achieved at a current density of 400 milliamperes per square centimetre (at 1.5 volts versus a reversible hydrogen electrode) and a cathodic-side (half-cell) ethylene power conversion efficiency of 55 ± 2 per cent at 150 milliamperes per square centimetre. We perform computational studies that suggest that the Cu-Al alloys provide multiple sites and surface orientations with near-optimal CO binding for both efficient and selective CO_2 reduction[17]. Furthermore, in situ X-ray absorption measurements reveal that Cu and Al enable a favourable Cu coordination environment that enhances C–C dimerization. These findings illustrate the value of computation and machine learning in guiding the experimental exploration of multi-metallic systems that go beyond the limitations of conventional single-metal electrocatalysts.

To accelerate catalyst discovery, we developed a machine-learning-accelerated, high-throughput density functional theory (DFT) framework[18] to screen materials ab initio. We provided this framework with 244 different copper-containing intermetallic crystals from The Materials Project[25], from which we enumerated 12,229 surfaces and 228,969 adsorption sites. We then performed DFT simulations on a subset of these sites to calculate their CO adsorption energies (Supplementary Information). These data were used to train an machine learning model, which we used to predict CO adsorption energies on the adsorption sites. The framework then combined the machine-learning-predicted CO adsorption energies with volcano scaling relationships[17] to predict the most catalytically active sites, which have CO adsorption energies (ΔE_{CO}) near to −0.67 eV, a value predicted to produce near-optimal activity in the volcano scaling relationship (see Supplementary Information and Supplementary Figs. 1, 2 for details on calculating the optimal ΔE_{CO} of −0.67 eV). These optimal sites were simulated using DFT to provide additional training data for the machine learning model. Cycling among DFT simulation, machine learning regression and machine learning prioritization yielded an automated framework that systematically searched for surfaces and adsorption sites with near-optimal CO adsorption energies. In total, the framework carried out about 4,000 DFT simulations, yielding a set of candidates for experimental testing.

Of the candidate materials identified, we found Cu-Al to be the most promising for active and selective CO_2 reduction. We created two-dimensional activity and selectivity volcano plots for CO_2 reduction

[1]Department of Electrical and Computer Engineering, University of Toronto, Toronto, Ontario, Canada. [2]College of Engineering and Applied Sciences, National Laboratory of Solid State Microstructures, Collaborative Innovation Center of Advanced Microstructure, Nanjing University, Nanjing, China. [3]Chemical Engineering, Carnegie Mellon University, Pittsburgh, PA, USA. [4]Materials Science Engineering, University of Toronto, Toronto, Ontario, Canada. [5]Ontario Centre for Characterization of Advanced Materials (OCCAM), University of Toronto, Toronto, Ontario, Canada. [6]National Synchrotron Radiation Laboratory, University of Science and Technology of China, Hefei, China. [7]Industrial Technology Research Institute, Material and Chemical Research Laboratories, Hsinchu, Taiwan. [8]Present address: National Research Council of Canada, Ottawa, Ontario, Canada. [9]These authors contributed equally: Miao Zhong, Kevin Tran, Yimeng Min, Chuanhao Wang. ✉e-mail: zulissi@andrew.cmu.edu; ted.sargent@utoronto.ca

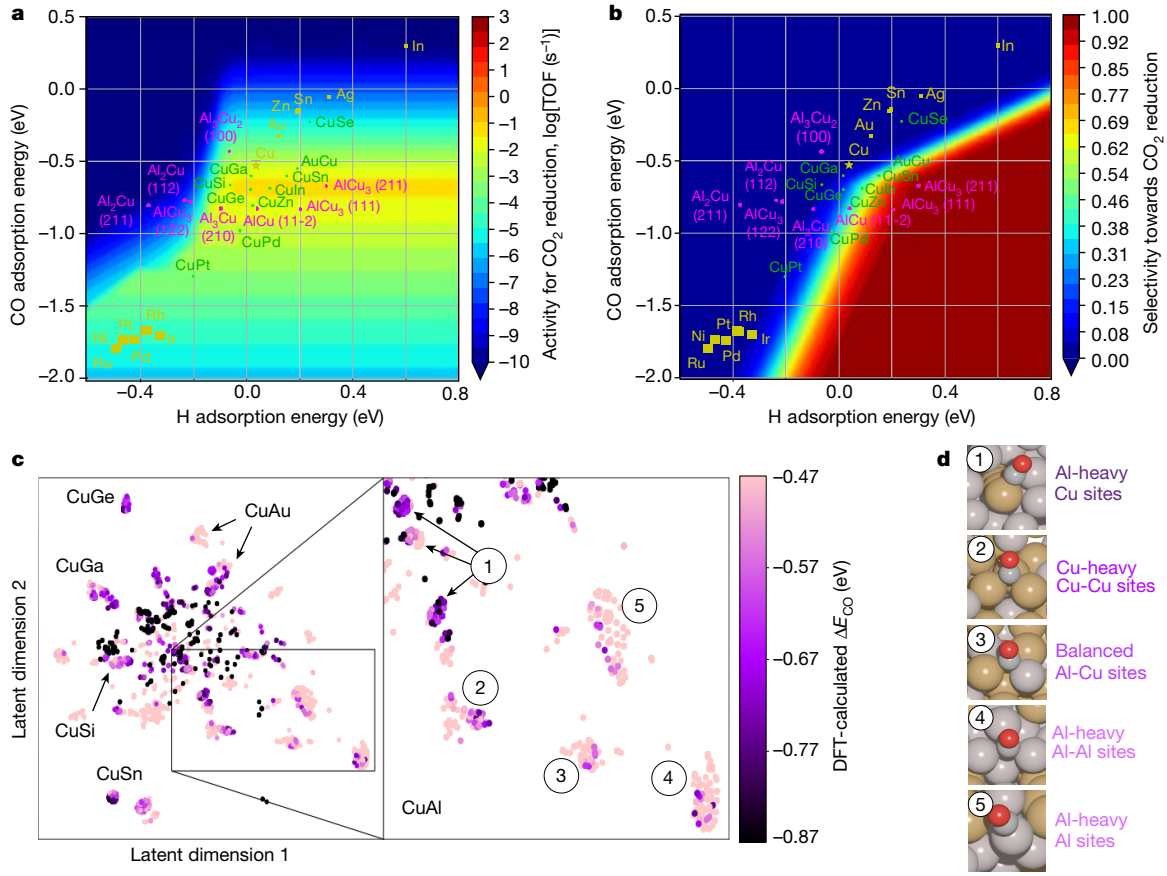

Fig. 1 | Screening of Cu and Cu based compounds using computational methods. a, A two-dimensional activity volcano plot for CO_2 reduction. TOF, turnover frequency. **b**, A two-dimensional selectivity volcano plot for CO_2 reduction. CO and H adsorption energies in panels **a** and **b** were calculated using DFT. Yellow data points are average adsorption energies of monometallics; green data points are average adsorption energies of copper alloys; and magenta data points are average, low-coverage adsorption energies of Cu-Al surfaces. **c**, *t*-SNE[19] representation of approximately 4,000 adsorption sites on which we performed DFT calculations with Cu-containing alloys. The Cu-Al clusters are labelled numerically. **d**, Representative coordination sites for each of the clusters labelled in the *t*-SNE diagram. Each site archetype is labelled by the stoichiometric balance of the surface, that is, Al-heavy, Cu-heavy or balanced, and the binding site of the surface.

(Fig. 1a, b)[17,26] (Supplementary Information and Supplementary Fig. 3). Figure 1a shows that a CO binding energy near −0.67 eV is required for high activity. It also shows that, given a CO binding energy of about −0.67 eV, a H binding energy above approximately −0.5 eV is required for activity and that a H binding energy above approximately −0.2 eV is required for selectivity towards CO_2 reduction instead of H_2 evolution (Fig. 1a, b).

Since these criteria were met by multiple copper alloy candidates, we pared the list of candidates by visualizing and analysing them in a *t*-SNE diagram[19] (Fig. 1c). Each point on this diagram represents one adsorption site for which we performed a DFT calculation. Points near to one other tend to have similar coordination atoms and surface compositions (Supplementary Information). Clusters of sites represent therefore different adsorption site archetypes (Fig. 1d). Figure 1c shows that Cu-Al exhibits the highest abundance of adsorption sites and site types with near-optimal ΔE_{CO} values, suggesting that Cu-Al alloys may be active across a relatively wide range of surface compositions and site types. The zoomed-in *t*-SNE diagram with example adsorption sites (Fig. 1d) reveals that Al sites tend to bind CO too weakly; Cu sites surrounded by mostly Al atoms may bind CO too strongly; and Cu-Al bridge sites surrounded mostly by Cu atoms are predicted to be active. The low abundance of low ΔE_{CO} sites in Cu-Al alloys also suggests that Cu-Al may be resistant to CO over-binding. We conclude that Cu-Al alloys with a higher Cu content than Al are of potential interest for CO_2 reduction.

To test these hypotheses, we prepared experimentally a suite of Cu-Al model catalysts: ion-implanted Al-on-Cu and evaporated-and-etched Al-on-Cu (see Methods and Supplementary Fig. 4). Each catalyst shows a morphology similar to that of an evaporated pure Cu catalyst (Supplementary Figs. 5–7). Compared with the pure Cu catalyst, which attained a C_2H_4 Faradaic efficiency of 35% at a current density of 600 mA cm^{-2} in a 1 M KOH electrolyte in a flow-cell configuration (Supplementary Fig. 8), both ion-implanted and evaporated-and-etched Al-on-Cu catalysts exhibited higher C_2H_4 Faradaic efficiencies of about 60% under the same testing conditions. The CO Faradaic efficiencies on both Cu-Al catalysts were suppressed to about 10%, one-third of that obtained using pure Cu (Supplementary Fig. 9). Incorporating Al on Cu thus increased selectivity towards C_2H_4. Al-on-Cu catalysts maintained about 60% C_2H_4 over 5 h. The Tafel slopes of C_2H_4 production (Supplementary Fig. 9) for pure Cu, ion-implanted, and evaporated-and-etched Al-on-Cu catalysts are 180, 147 and 145 mV per decade, respectively, further highlighting the faster C–C dimerization kinetics with Al-on-Cu catalysts.

To estimate quantitatively the amount of Al incorporated near the Cu surface, we used surface-sensitive Auger electron spectroscopic analysis (Supplementary Figs. 10, 11). This method provides compositional information about the top 1–3 nm of the samples and does so over a relatively large area (100 μm^2 in our studies)[20]. We estimated that the molar concentrations of Al on surfaces are 4.5% and 25% for the ion-implanted and evaporated-and-etched Al-on-Cu, respectively. Scanning electron microscopy (SEM) and X-ray spectroscopy analyses

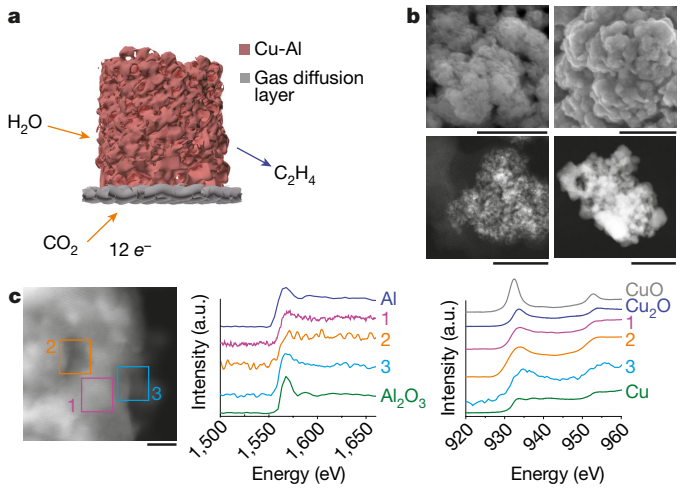

Fig. 2 | Schematic and characterization of de-alloyed Cu-Al catalyst. **a**, Schematic of a de-alloyed nanoporous Cu-Al catalyst on a gas diffusion layer for CO_2 electroreduction. **b**, SEM and HAADF-STEM images of de-alloyed Cu-Al catalyst before (left) and after (right) CO_2 electroreduction. The scale bars for the SEM images are 500 nm (top left) and 200 nm (top right). The scale bars for the TEM images are 200 nm (bottom left) and 100 nm (bottom right). **c**, HAADF-STEM image and EELS spectra of the de-alloyed Cu-Al catalyst. Curves numbered 1, 2 and 3 in the EELS spectra represent the EELS results measured at areas 1, 2 and 3 in the corresponding HAADF-STEM image. Al, Al_2O_3, CuO, Cu_2O and Cu EELS results are plotted as references. The scale bar is 5 nm. a.u., arbitrary units.

confirmed no major change of morphologies or Al concentrations for the ion-implanted and evaporated-and-etched Al-on-Cu samples before and after 5 h of CO_2 reduction (Supplementary Figs. 6, 7, 12–15). (See Supplementary Information and Supplementary Figs. 16–19 for detailed operating stability information.) Pourbaix diagrams[21] (Supplementary Fig. 20) show that both Cu and Al are cathodically protected at potentials more negative than their oxidation potentials of −1.4 V versus a reversible hydrogen electrode (RHE) in a pH 14 electrolyte.

We sought therefore to develop a further optimized Cu-Al catalyst. We explored both thermal evaporation and co-sputtering followed by chemical etching to synthesize de-alloyed nanoporous Cu-Al catalysts (Supplementary Information). As shown in SEM and high-angle angular dark field-scanning transmission electron microscopy (HAADF-STEM) images (Fig. 2b and Supplementary Fig. 21), a nanoporous structure with pore sizes of 5–20 nm was formed. Compared to ion-implanted and evaporated-and-etched Al-on-Cu catalysts, the de-alloyed nanoporous Cu-Al catalysts may offer a higher geometric density of catalytically active sites for adsorption and electroreduction of CO_2. After 5 h of CO_2 electroreduction at a current density of 600 mA cm^{-2}, the grain size increased, potentially owing to surface reconstruction of Cu and Al in the electrolyte during the reaction (Fig. 2b). Energy-dispersive X-ray spectroscopy analyses in transmission electron microscopy (TEM) and SEM, electron energy loss spectroscopy (EELS) spectra, and elemental mapping in STEM indicated a homogeneous distribution of Al and Cu in de-alloyed catalysts before and also after 5 h of reaction (Fig. 2c and Supplementary Figs. 22–25). We performed HAADF-STEM analysis and found that Cu (111) and (200) facets were observed with interplanar spacings of 0.211 nm and 0.182 nm (Supplementary Fig. 26). Auger electron spectroscopic analysis revealed about 9% Al on the surface following the reaction (Supplementary Figs. 27 and 28).

Given the presence of Cu (111) and (100) surfaces, we used the machine learning model and DFT calculations to analyse how the ratio of Al to Cu on these surfaces affects ΔE_{CO}. First, we enumerated (using Delaunay triangulation[22]) the range of adsorption sites on the Cu (111) surfaces having different Al concentrations; and then predicted ΔE_{CO} for these sites using the machine learning model, thus creating a distribution of ΔE_{CO} values. We repeated this for the Cu (100) surfaces at different Al concentrations. The resulting distributions (Supplementary Fig. 29) show that adding about 12% Al to the Cu (111) surface maximizes the density of sites with ΔE_{CO} values near the optimum of −0.67 eV and that adding 4–12% Al maximizes the density of sites optimal for the Cu (100) surface.

We carried out DFT calculations over the best machine-learning-predicted structures to characterize the changes in reaction energies in the major steps during CO_2 reduction. The reaction energy in the rate-determining step of C–C bond-making[12] decreased from 1.4 eV to 0.6 eV on Cu (111) and from 0.6 eV to 0.4 eV on Cu (100) with the benefit of Al incorporation (Supplementary Figs. 30–33). The DFT results show that the reaction energy of the C–C coupling step (the rate-determining step in the electrochemical CO_2-to-C2 conversion) is lower for the Cu-Al surfaces compared to that for the corresponding pure Cu surfaces. The DFT results further showed that the reaction energy for forming HO(CH)CH, an intermediate of ethanol[23], was higher than that for forming CCH, an intermediate of C_2H_4 (ref. [23]) with Al-containing Cu (Supplementary Fig. 34). Water near the Al atoms may assist the reduction of HOCCH to CCH instead of hydrogenation of HOCCH to HO(CH)CH[23]. Thus, the alcohol was suppressed and C_2H_4 production was promoted.

We then systematically evaluated the CO_2 electroreduction performance of the de-alloyed Cu-Al catalysts on carbon-based gas diffusion layer (C-GDL) substrates with about 10% Al at the surfaces at current densities of 200–800 mA cm^{-2} in 1 M KOH in flow cells (Fig. 3a and 3b). To quantify the Faradaic efficiencies for each product, we carried out CO_2 electroreduction in the chronopotentiometry mode. As shown in Fig. 3b, we achieved C_2H_4 Faradaic efficiency of 80% at a current density of 600 mA cm^{-2}. This is a twofold increase compared to the 35% Faradaic efficiency of pure Cu measured under the same conditions. A CO_2-to-C_2H_4 half-cell power conversion efficiency (PCE) in a full-cell $CO_2 + H_2O$-to-$C_2H_4 + O_2$ reaction (half-cell C_2H_4 PCE) of 34% was achieved (Fig. 3d), which is similar to the previously published highest half-cell C_2H_4 PCE of about 30% using a plasma-activated copper electrocatalyst[13] with a C_2H_4 Faradaic efficiency of 60%. This prior work has a much lower current density of around 12 mA cm^{-2} in the same electrolyte. An average C_2H_4 Faradaic efficiency of 75 ± 4% was obtained over 17 de-alloyed distinct Cu-Al on C-GDL samples (about 10% Al on the surfaces) at a current density of 600 mA cm^{-2}. Overall C_{2+} (multi-carbon product) production Faradaic efficiency was 85–90% when we used the de-alloyed Cu-Al catalyst, higher than the 55–60% using the flat Cu catalyst (Fig. 3c and Supplementary Fig. 9).

We further designed control catalysts—nanoporous Cu on C-GDL with a very low amount of Al on the surface and having similar nanoporosity to that of the de-alloyed Cu-Al catalyst—to clarify the role of morphology (see Methods, Supplementary Information and Supplementary Figs. 35–36). Auger electron spectroscopy analysis revealed that surface Al was a low 2–3% (Supplementary Fig. 37). The C_2H_4 Faradaic efficiency was decreased to 53% at the same current of 600 mA cm^{-2} (Fig. 3b and Supplementary Fig. 38).

The Cu-Al on C-GDL catalysts exhibited stable potentials between −1.8 V and −2.1 V versus RHE and a C_2H_4 Faradaic efficiency of 75% over 5 h of continuous operation at 600 mA cm^{-2} (Supplementary Fig. 39). After 5 h, the C-GDL gradually lost its hydrophobicity and became flooded with 1 M KOH electrolyte[3]. CO_2 could therefore no longer diffuse to the catalyst surface for CO_2 reduction.

To improve device stability, we fabricated de-alloyed Cu-Al catalysts on polytetrafluoroethylene (PTFE) substrates whose hydrophobicity is stable over extended operation in a strong alkaline electrolyte[3] (Supplementary Information, and Supplementary Figs. 21, 40 and 41). Carbon nanoparticles/graphite were coated on the de-alloyed Cu-Al surface to create a sandwich structure that would distribute the current uniformly over the catalyst to stabilize its surface during

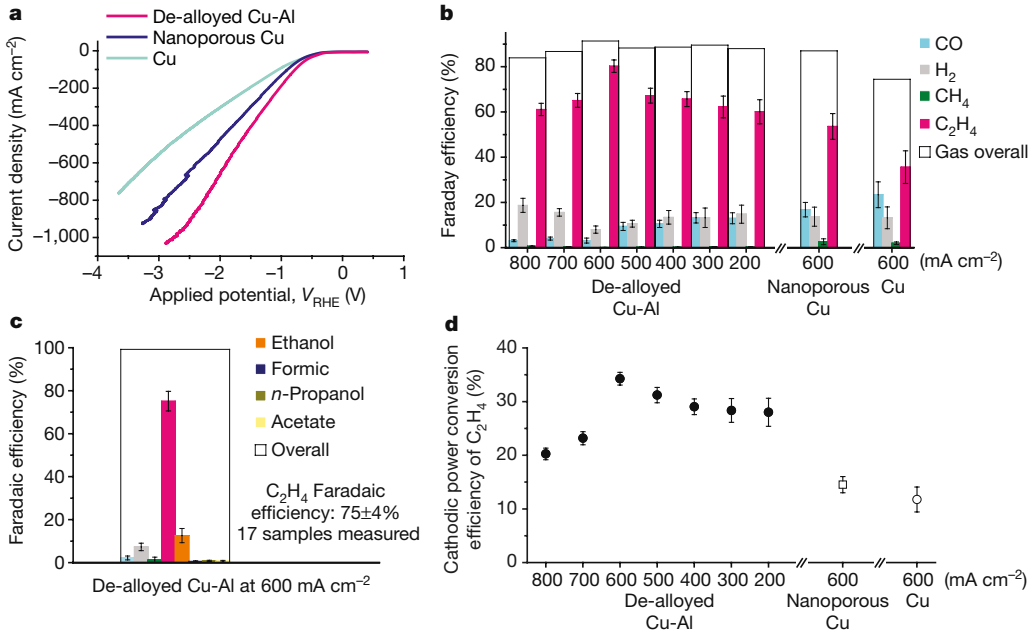

Fig. 3 | CO_2 electroreduction performance on de-alloyed Cu-Al, porous Cu and deposited Cu catalysts on C-GDL substrates in 1 M KOH electrolytes. **a**, C_2H_4 production current density versus potential with de-alloyed Cu-Al, nanoporous Cu and evaporated Cu catalysts. **b**, Faradaic efficiencies for gaseous products with de-alloyed Cu-Al catalysts at different applied current densities and with nanoporous Cu and evaporated Cu catalysts at a constant current density of 600 mA cm^{-2} obtained using chronopotentiometry. The error bars represent one standard deviation based on five independent samples measured. **c**, Faradaic efficiencies for all products at an applied current density of 600 mA cm^{-2} with 17 de-alloyed Cu-Al samples measured. **d**, Half-cell CO_2-to-C_2H_4 power conversion efficiency with de-alloyed Cu-Al catalysts at different applied current densities and with nanoporous Cu and evaporated Cu catalysts at a constant current density of 600 mA cm^{-2} obtained using chronopotentiometry. The error bars represent one standard deviation based on five independent samples measured.

reaction[3]. As shown in Fig. 4b, c and Supplementary Fig. 42, we achieved C_2H_4 Faradaic efficiencies over 80% in 1 M KOH at a current density of 400 mA cm^{-2}. Commercial electrolysers require current densities exceeding 0.2 A cm^{-2} for capital costs to be acceptable[33]. Compared to the previous best[3], we achieved a 2.8× advance in cathodic PCE at 400 mA cm^{-2} using Cu-Al. We demonstrated over 100 h of stability at this best condition (Supplementary Figs. 64, 65 and 67).

To improve the overall energy conversion efficiency, we studied Cu-Al performance under different pH conditions[27]. Experimentally, we found that 3 M KOH (pH 14.5) allowed us to reach 48–52% half-cell C_2H_4 PCE at a current density of 150 mA cm^{-2} and was stable over 50 h (Fig. 4b, d). We then optimized the cation concentration by adding an additional 3 M KI into the electrolyte. KI was chosen because the K^+ cation and I^- anion are known to increase CO_2 reduction activity by accelerating the hydrogenation of the key adsorbed CO intermediate[3,28]. This further diminished the CO Faradaic efficiency to below 0.3% and reduced H_2 production by 3%, increasing the C_2H_4 Faradaic efficiency to 73 ± 4%. As a result, we achieved a 55 ± 2% half-cell C_2H_4 PCE (over ten distinct samples) at 150 mA cm^{-2} (Fig. 4b, Supplementary Figs. 43 and 63). Note that the cathodic-side half-cell PCE captures the cathodic CO_2 reduction performance only, and it also does not depend on the location of the reference potential (versus RHE or versus a standard hydrogen electrode, SHE; see the potential diagram in Supplementary Fig. 63). Therefore, the half-cell PCE is useful to compare the energy efficiency on one side of a full-cell reaction[30–32]. This energy conversion efficiency was stable over 50 h of CO_2 reduction operation. The improved half-cell C_2H_4 PCE in 3 M KOH and 3 M KI electrolytes may benefit from at least one of the following contributions: (1) Al as modulator with Cu to create more active CO_2 reduction sites, (2) the highly nanotextured catalyst surface[29], (3) the electrolyte effect from OH^-, K^+ and I^-, all of which are known to increase CO_2 reduction activity[3,27,28].

We compare the performance of the de-alloyed Cu-Al/PTFE catalyst with that of the abrupt-interface Cu/PTFE catalyst[3] under identical CO_2 electrolysis conditions. The de-alloyed Cu-Al/PTFE catalyst shows improved Faradaic efficiency and half-cell C_2H_4 PCE under all measured conditions (Supplementary Figs. 64, 65). We note that optimization of electrolysis conditions is crucial to enable Cu-Al to achieve its best CO_2-to-C_2H_4 performance. We also plot the performance of the Cu-Al catalyst compared with that of the previous most efficient abrupt-interface Cu catalyst[3] in the reported techno-economic analysis (Supplementary Fig. 66). The Cu-Al catalyst brings the performance into the break-even region; this is an improvement on access to only the below-break-even region in the previous most efficient C_2H_4 electroproduction results.

No obvious leaching of Al and Cu into the solution was observed via inductively coupled plasma atomic emission spectroscopy (ICP-AES) analysis (Supplementary Fig. 44). The concentrations of Cu and Al at time zero are the Cu and Al concentrations in the KOH electrolyte without performing CO_2 electrolysis. Therefore, the detected small amount of Cu and Al in the solutions are impurities from KOH catholyte, which also shows no major change during the reaction, indicating a stable electrolysis system. We further confirmed that the assumed dissolved amounts of Cu and Al from Cu-Al to solution is far below 1% compared to impurity levels in the solution (Supplementary Information).

To investigate the Cu-Al catalyst further, we performed in situ synchrotron X-ray absorption near-edge structure (XANES) analysis under the same testing conditions (see Supplementary Information and Supplementary Fig. 45). Cu-O bonding was observed via both ex situ and in situ XANES analyses with the de-alloyed Cu-Al catalyst before, during and after the reaction[24]. We used DFT to analyse the reaction energy changes when O is placed on the top surface or in the subsurface of the machine learning-predicted Cu-Al models. The reaction energies in the rate-determining steps in the CO_2 reduction are lower with O in the Cu-Al compared to that of pure Cu (Supplementary Figs. 46–61 and Supplementary Tables 1–8). The XANES spectra of Al in the Cu-Al sample before and after the reaction are shown in Supplementary Fig. 62.

To conclude, we have developed a Cu-Al catalyst for active and selective CO_2 electroreduction to C_2H_4. We demonstrate the

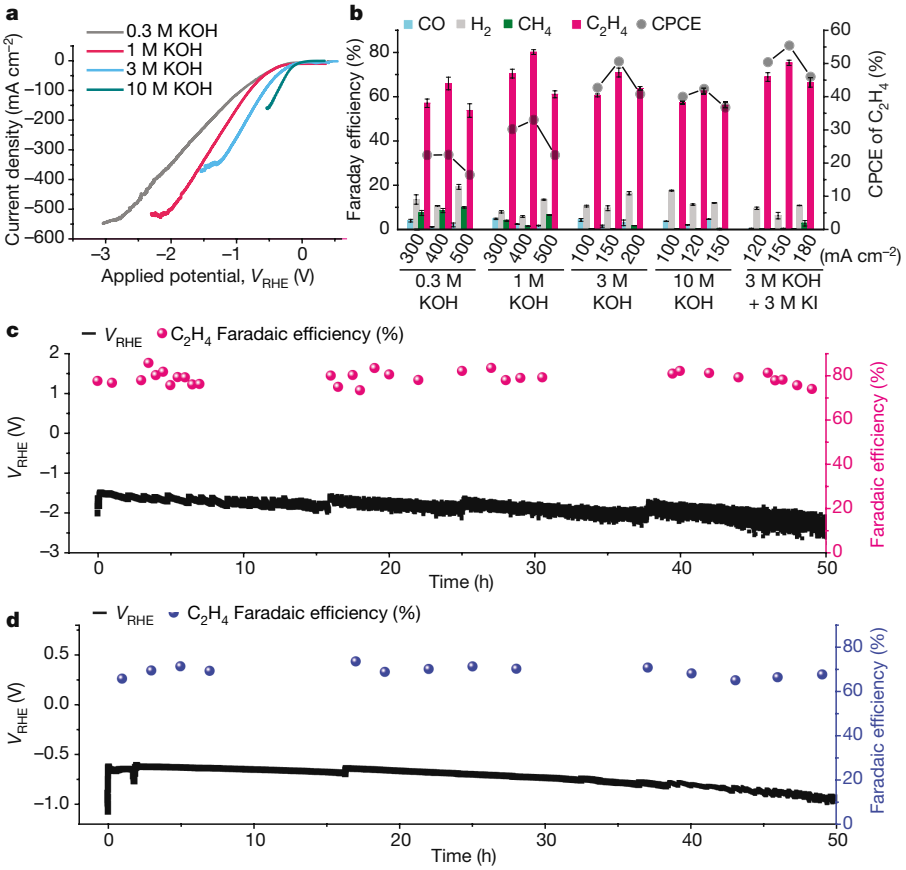

Fig. 4 | CO_2 electroreduction performance on de-alloyed Cu-Al catalysts on PTFE substrates in alkaline electrolytes at different pH values. a, C_2H_4 production current density versus potential with de-alloyed Cu-Al in 0.3 M, 1 M, 3 M and 10 M KOH electrolytes. **b**, Faradaic efficiencies for gaseous products with its corresponding C_2H_4 power conversion efficiencies of the de-alloyed Cu-Al catalysts in the different electrolytes and at different applied current densities. The error bars for Faradaic efficiencies measured in 0.3 M and 10 M electrolytes represent one standard deviation based on five independent samples measured. The error bars for Faradaic efficiencies measured in 1 M KOH, 3 M KOH and 3 M KOH + 3 M KI electrolytes represent one standard deviation based on ten independent samples measured. **c**, The CO_2 electroreduction stability of the carbon nanoparticles/de-alloyed Cu-Al/PTFE electrode in a 1 M KOH electrolyte at an applied current density of 400 mA cm^{-2}. The left axis shows potential (versus RHE; V) versus time (s); the right axis shows C_2H_4 Faradaic efficiency (%) versus time (s). **d**, The CO_2 electroreduction stability of the carbon nanoparticles/de-alloyed Cu-Al/PTFE electrode in a 3 M KOH electrolyte at an applied current density of 150 mA cm^{-2}. The left axis shows potential (versus RHE; V) versus time (s); the right axis shows C_2H_4 Faradaic efficiency (%) versus time (s). Note that we passed a small amount of 1 M KI catholyte (pH 5.5–6.5) as a buffer electrolyte before passing the KOH catholyte to protect the Cu-Al catalyst from any possible dissolution into the KOH catholyte. The small amount of KI was then pumped out of the flow-cell system after use as a buffer electrolyte. We convert the potential to V_{RHE} using the equation: $V_{RHE} = V_{Ag/AgCl} + 0.199 + 0.059 \times pH$, in which we use the testing KOH catholyte pH values for calculation. The potentials at time 0 in panels **c** and **d** should be approximately −0.5 V more cathodic. CPCE, cathodic power conversion efficiency.

prediction of promising electrocatalysts by combining volcano relationships, DFT and active machine learning to optimize catalyst performance. The findings suggest avenues towards multi-metal catalysts that outperform single-component catalysts by using an intermediate-binding-optimization and reaction-electrolyte-optimization strategy for multi-carbon production via CO_2 electroreduction.

Online content

Any methods, additional references, Nature Research reporting summaries, source data, extended data, supplementary information, acknowledgements, peer review information; details of author contributions and competing interests; and statements of data and code availability are available at https://doi.org/10.1038/s41586-020-2242-8.

1. Lin, S. et al. Covalent organic frameworks comprising cobalt porphyrins for catalytic CO_2 reduction in water. *Science* **349**, 1208–1213 (2015).
2. Schreier, M. et al. Solar conversion of CO_2 to CO using Earth-abundant electrocatalysts prepared by atomic layer modification of CuO. *Nat. Energy* **2**, 17087 (2017).
3. Dinh, C. et al. Sustained high-selectivity CO_2 electroreduction to ethylene via hydroxide-mediated catalysis at an abrupt reaction interface. *Science* **360**, 783–787 (2018).
4. Li, C. et al. Electroreduction of carbon monoxide to liquid fuel on oxide-derived nanocrystalline copper. *Nature* **508**, 504–507 (2014).
5. Lu, Q. et al. A selective and efficient electrocatalyst for carbon dioxide reduction. *Nat. Commun.* **5**, 3242 (2014).
6. Gao, S. et al. Partially oxidized atomic cobalt layers for carbon dioxide electroreduction to liquid fuel. *Nature* **529**, 68–71 (2016).
7. Li, Y. C. et al. Electrolysis of CO_2 to syngas in bipolar membrane-based electrochemical cells. *ACS Energy Lett.* **1**, 1149–1153 (2016).
8. Jeanty, P. et al. Upscaling and continuous operation of electrochemical CO_2 to CO conversion in aqueous solutions on silver gas diffusion electrodes. *J. CO_2 Util.* **24**, 454–462 (2018).
9. Hori, Y. et al. Selective formation of C2 compounds from electrochemical reduction of CO_2 at a series of copper single crystal electrodes. *J. Phys. Chem. B* **106**, 15–17 (2002).
10. Yano, H. et al. Selective electrochemical reduction of CO_2 to ethylene at a three-phase interface on copper(I) halide-confined Cu-mesh electrodes in acidic solutions of potassium halides. *J. Electroanal. Chem.* **565**, 287–293 (2004).
11. Peterson, A. A. et al. How copper catalyzes the electroreduction of carbon dioxide into hydrocarbon fuels. *Energy Environ. Sci.* **3**, 1311–1315 (2010).
12. Kortlever, R. et al. Catalysts and reaction pathways for the electrochemical reduction of carbon dioxide. *J. Phys. Chem. Lett.* **6**, 4073–4082 (2015).
13. Mistry, H. et al. Highly selective plasma-activated copper catalysts for carbon dioxide reduction to ethylene. *Nat. Commun.* **7**, 12123 (2016).

14. Li, Y. et al. Structure-sensitive CO_2 electroreduction to hydrocarbons on ultrathin 5-fold twinned copper nanowires. *Nano Lett*. **17**, 1312–1317 (2017).
15. Lum, Y. et al. Optimizing C–C coupling on oxide-derived copper catalysts for electrochemical CO_2 reduction. *J. Phys. Chem. C* **121**, 14191–14203 (2017).
16. De Luna, P. et al. Catalyst electro-redeposition controls morphology and oxidation state for selective carbon dioxide reduction. *Nat. Catal*. **1**, 103–110 (2018).
17. Liu, X. et al. Understanding trends in electrochemical carbon dioxide reduction rates. *Nat. Commun*. **8**, 15438 (2017).
18. Tran, K. et al. Active learning across intermetallics to guide discovery of electrocatalysts for CO_2 reduction and H_2 evolution. *Nat. Catal*. **1**, 696–703 (2018).
19. van der Maaten, L. Accelerating *t*-SNE using tree-based algorithms. *J. Mach. Learn. Res*. **15**, 3221–3245 (2014).
20. Davis, L. E. et al. *Handbook of Auger Electron Spectroscopy* 2nd edn (Physical Electronics Industries, 1976).
21. Persson, K. A. et al. Prediction of solid-aqueous equilibria: scheme to combine first-principles calculations of solids with experimental aqueous states. *Phys. Rev. B* **85**, 235438 (2012).
22. Montoya, J. H. et al. A high-throughput framework for determining adsorption energies on solid surfaces. *npj Comput. Mater*. **3**, 14 (2017).
23. Xiao, H. et al. Atomistic mechanisms underlying selectivities in C1 and C2 products from electrochemical reduction of CO on Cu (111). *J. Am. Chem. Soc*. **139**, 130–136 (2017).
24. Xiao, H. et al. Cu metal embedded in oxidized matrix catalyst to promote CO_2 activation and CO dimerization for electrochemical reduction of CO_2. *Proc. Natl Acad. Sci. USA* **114**, 6685–6688 (2017).
25. Jain, A. et al. The Materials Project: a materials genome approach to accelerated materials innovation. *APL Mater*. **1**, 011002 (2013).
26. Nørskov, J. K. et al. Trends in the exchange current for hydrogen evolution. *J. Electrochem. Soc*. **152**, J23–J26 (2005).
27. Wang, L. et al. Electrochemical carbon monoixde reduction on polycrystalline copper: effects of potential, pressure, and pH on selectivity toward multicarbon and oxygenated products. *ACS Catal*. **8**, 7445–7454 (2018).
28. Liu, M. et al. Enhanced electrocatalytic CO_2 reduction via field-induced reagent concentration. *Nature* **537**, 382–386 (2016).
29. Zeng, Z. *et al*. Stabilization of ultrathin (hydroxy)oxide films on transition metal substrates for electrochemical energy conversion. *Nat. Energy* **2**, 17070 (2017).
30. She, Z. W. *et al*. Combining theory and experiment in electrocatalysis: Insights into materials design. *Science* **355**, 146 (2017).
31. Larrazábal, G. O. et al. Building blocks for high performance in electrocatalytic CO2 reduction: materials, optimization strategies, and device engineering. *J. Phys. Chem. Lett*. **8**, 3933–3944 (2017).
32. Whipple, D. T. et al. Prospects of CO_2 utilization via direct heterogeneous electrochemical reduction. *J. Phys. Chem. Lett*. **1**, 3451–3458 (2010).
33. De Luna, P. et al. What would it take for renewably powered electrosynthesis to displace petrochemical processes? *Science* **364**, eaav3506 (2019).

Data availability

Source data to generate figures and tables are available from the corresponding authors on reasonable request.

Code availability

Code to generate figures and tables is available from the corresponding authors on reasonable request.

Acknowledgements This work was supported financially by the Ontario Research Fund Research-Excellence Program, the Natural Sciences and Engineering Research Council (NSERC) of Canada, the Canadian Institute for Advanced Research (CIFAR) Bio-Inspired Solar Energy programme, the University of Toronto Connaught programme, and TOTAL American Services. M.Z. thanks the National Natural Science Foundation of China (grant number 91963121), and S. Tolbert from the University of California, Los Angeles for discussions of de-alloying. S.S. thanks the National Key Research and Development Program of China (grant number 2016YFB0700205) and the National Natural Science Foundation of China (grant number U1632273). We thank R. Morris and D. Sinton from the University of Toronto for discussions. We thank C. McCallum, R. Wolowiec, D. Kopilovic, S. Boccia, A. Ip, M. Liu, Y. Pang, M. Askerka, A. Seifitokaldani, T. T. Zhuang and Z. Liang from the University of Toronto, Canada and C.-W. Huang, L.-J. Chen from National Tsing Hua University, Taiwan, for their help during the course of study. We thank the beamline scientists from the Source optimisée de lumière d'énergie intermédiaire du LURE (SOLEIL) Synchrotron in France for performing in situ X-ray absorption analyses. This research used resources of the National Energy Research Scientific Computing Center, a Department of Energy (DOE) Office of Science User Facility supported by the Office of Science of the US Department of Energy under contract number DE-AC02-05CH11231. Computations were performed on the Southern Ontario Smart Computing Innovation Platform (SOSCIP) Consortium's Blue Gene/Q computing platform. SOSCIP is funded by the Federal Economic Development Agency of Southern Ontario, the Province of Ontario, IBM Canada Ltd, Ontario Centres of Excellence, MITACS and 15 Ontario academic member institutions.

Author contributions E.H.S. supervised the project. M.Z. and E.H.S. conceived the idea. M.Z. and C.W. designed and carried out the experiments. K.T., Z.Y. and Z.U. performed the machine learning studies. K.T., Z.Y., Z.U., Y.M., Z.W. O.V., P.D.L., M.A., M.Z. and E.H.S. discussed the machine learning results. Y.M., Z.W. O.V., P.D.L., M.A., A.S., F.C., K.T., Z.Y. and Z.U. carried out the DFT simulations. P.B. carried out the Auger electron spectroscopy analyses. S.S. and P.D.L. performed X-ray absorption spectroscopy measurements. C.-S.T. and S.-C.L. carried out the TEM analyses. C.-T.D., A.S.R., C.-S.T., M.A., M.L., A.S., Y.P. and A.I. contributed to the discussion of the results. All authors discussed the results and assisted during manuscript preparation.

Competing interests The authors declare no competing interests.

Additional information
Supplementary information is available for this paper at https://doi.org/10.1038/s41586-020-2242-8.
Correspondence and requests for materials should be addressed to Z.U. or E.H.S.
Peer review information *Nature* thanks Hailiang Wang and the other, anonymous, reviewer(s) for their contribution to the peer review of this work.
Reprints and permissions information is available at http://www.nature.com/reprints.